First principles multielectron mixed quantum/classical simulations in the condensed phase. II. The charge-transfer-to-solvent states of sodium anions in liquid tetrahydrofuran

William J. Glover, Ross E. Larsen, and Benjamin J. Schwartz[a)]
Department of Chemistry and Biochemistry, University of California, Los Angeles, Los Angeles, California 90095-1569, USA

(Received 19 November 2009; accepted 12 January 2010; published online 8 April 2010)

Gas-phase atomic anions lack bound electronic excited states, yet in solution many of these anions exhibit intense absorption bands due to the presence of excited states, referred to as charge-transfer-to-solvent (CTTS) states that are bound only by the presence of the solvent. CTTS spectra thus serve as delicate probes of solute-solvent interactions, but the fact that they are created by the interactions of a solute with many solvent molecules makes them a challenge to describe theoretically. In this paper, we use mixed quantum/classical molecular dynamics with the two-electron Fourier-grid (2EFG) electronic structure method presented in the previous paper [W. J. Glover, R. E. Larsen, and B. J. Schwartz, J. Chem. Phys. **132**, 144101 (2010)] to simulate the CTTS states of a sodium anion in liquid tetrahydrofuran, Na^-/THF. Since our 2EFG method is based on configuration interaction with single and double excitations in a grid basis, it allows for an exact treatment of the two valence electrons of the sodium anion. To simulate Na^-/THF, we first develop a new electron–THF pseudopotential, and we verify the accuracy of this potential by reproducing the experimental absorption spectrum of an excess electron in liquid THF with near quantitative accuracy. We also are able to reproduce the CTTS spectrum of Na^-/THF and find that the CTTS states of Na^- exhibit a Rydberg-like progression due to the pre-existing long-range solvent polarization around the anion. We also find that the CTTS states are highly mixed with the disjoint electronic states supported by naturally occurring solvent cavities that exist in liquid THF. This mixing explains why the solvated electrons that are ejected following CTTS excitation appear with their equilibrium absorption spectrum. The mixing of the CTTS and solvent-cavity states also explains why the recombination of the electron and its geminate Na^0 partner occurs on slower time scales when photoexciting in the blue compared to in the red of the CTTS band: blue excitation accesses CTTS states whose charge densities lies further from the position of the anion, whereas red excitation accesses CTTS states that lie primarily within the anion's first solvation shell. Finally, we see that the radial character of the CTTS states near the Na^+ core matches that of Na^0, explaining why the spectrum of this species appears instantly after photoexciting Na^-. © *2010 American Institute of Physics*. [doi:10.1063/1.3352565]

I. INTRODUCTION

In the preceding paper,[1] hereafter referred to as Paper I, we presented a Fourier-grid method for solving the time-independent Schrödinger equation for two-electron systems. We showed that this two-electron Fourier-grid (2EFG) method is particularly suited for implementation in mixed quantum/classical (MQC) molecular dynamics (MD) algorithms. As a first application of our 2EFG method to a condensed-phase problem, in this paper we examine the electronic states of a solution-phase two-electron atomic anion. The electronic excited states of dissolved atomic anions are of interest because they are unbound in the gas-phase: the electronic excited states are stabilized only because of interactions with the solvent, giving rise to an intense absorption band between the ground and the solvent-bound excited states.[2,3] Photoexcitation to these solvent-bound electronic excited states is followed by rapid ejection of an electron from the anion into the solvent to form a solvated electron.[4–7] Because electrons are ejected from these low-lying solvent-supported excited electronic states, they have been labeled charge-transfer-to-solvent (CTTS) states, and the nature of these states has been widely studied in both ultrafast pump-probe experiments[3,5–34] and theoretical calculations.[35–45] The theoretical calculations have demonstrated that a proper treatment of electronic exchange and correlation is critical to a correct description of CTTS states,[43,45] so our 2EFG method is perfectly suited for understanding the electronic structure and dynamics of such states.

The previous experimental and theoretical work on CTTS reactions has shown that the symmetry and energetics of the initially excited CTTS state are largely what determines the subsequent electron transfer dynamics.[3,21,27,43,44] In the case of the aqueous halides, the properties of the CTTS states are reasonably well understood. Quantum chemistry

a)Author to whom correspondence should be addressed. Electronic mail: schwartz@chem.ucla.edu.

calculations on aqueous iodide, I^-/H_2O, found that a single CTTS state arises from excitation of an iodide $5p$ electron into a solvent-supported s-like orbital localized mainly within the anion's first solvation shell.[43] The calculated I^- CTTS state had a binding energy of ~1.7 eV, which resulted primarily from the long-range solvent polarization created by the anionic solute.[43] The fact that only a single bound CTTS excited state is calculated for this system is in agreement with experimental results, which show that the electron ejection and subsequent recombination dynamics do not change as the excitation wavelength is tuned throughout the CTTS absorption band.[14]

In contrast, the properties of the excited states of sodide, Na^-, in solution are much less understood. The fact that the recombination dynamics subsequent to CTTS electron ejection varies with excitation wavelength[21] suggests that multiple electronic states reside under the main CTTS absorption band. On the basis of both polarized transient hole-burning experiments[33,46] and single-electron MQC MD simulations,[44] the CTTS band of Na^- in liquids has been assigned as arising from transitions from the ground state to three quasidegenerate p-like CTTS excited states whose energies are split by the locally asymmetric solvent environment.[47] We note, however, that the polarized transient bleach signal observed on the high-energy side of the Na^- CTTS spectrum[33] is not consistent with the interpretation of the spectrum being comprised of three orthogonally polarized p-like subbands.[29,48]

The situation with understanding the CTTS excited states of sodide in liquids is further complicated by the fact that both simulations[49,50] and experiments[27,29,31,51] have uncovered the presence of large voids in the liquid ethers in which Na^- is typically dissolved. The orientation of the solvent molecules surrounding these cavities typically favors the solvation of negatively charged objects such as electrons.[49,51] Thus, the presence of these naturally occurring solvent cavities gives rise to bound solvent-supported electronic states whether or not a solute is present: these electronic states are usually localized in one or more solvent cavities (and hence have been referred to as "disjoint states") and lie below the solvent conduction band in energy.[27,29,31,49,50] Coupling between these solvent-cavity-supported disjoint states and the anions' CTTS states has been invoked to rationalize the striking differences of the CTTS dynamics of iodide in water compared to iodide in liquid tetrahydrofuran (THF).[27,29] Moreover, pump-probe experiments on Na^- in THF and other ethers suggest that the solvent-supported disjoint states have an onset just above the lowest sodide CTTS state in energy;[27,31] this implies that the electronic structure of Na^- in ethers in the vicinity of the CTTS absorption maximum is likely more involved than the simple interpretation of three p-like CTTS states.

Thus, to further our understanding of the CTTS excited states of condensed-phase atomic anions, in this paper we explore the electronic structure of Na^- in liquid THF using the 2EFG method presented in Paper I. We chose to simulate the properties of sodide in THF because it is the solvent in which the Na^- CTTS reaction has been best studied experimentally[7,18–26,29–34] and thus affords the best possibilities for comparing theory to experiment. Moreover, because a proper treatment of exchange and correlation is crucial when simulating CTTS excited states,[43,45] our 2EFG method is perfectly suited to studying Na^-/THF because it affords an effectively exact (i.e., full CI) treatment of the two-valence-electron sodide electronic structure problem. Furthermore, because our 2EFG method uses a grid basis, it is capable of correctly describing the disjoint electronic states that occupy the naturally occurring voids in liquid THF; approaches based on atom-centered basis functions would be unable to describe these states without resorting to prohibitively large basis sets. Finally, our simulations are based on a MQC approach in which the classical solvent molecules dynamically respond to the quantum state of the solute's valence electrons, which is found at every MD time step.[45] This distinguishes our approach from quantum mechanics/molecular mechanics (QM/MM) methods that perform electronic structure calculations on solute-solvent configurations generated with approximate interactions from purely classical simulations.[43,52,53]

The rest of the paper is organized as follows. In Sec. II we outline our MQC simulation method and provide details of our Na^-/THF simulation model. Critical to our model is the development of a new pseudopotential to represent the electron–THF interaction; we validate our new pseudopotential by simulating the optical absorption spectrum of the solvated electron in THF, where we find excellent agreement with experiment. In Sec. III, we explore the properties of Na^-/THF's CTTS states with our 2EFG method. We find that although the lowest three CTTS states of sodide are indeed p-like, the presence of long-range solvent polarization, in combination with the naturally occurring solvent voids, leads to the existence of many additional bound CTTS states outside the anion's solvent cavity. These higher-lying CTTS states form a Rydberg-like progression, with s- and d-like states bound immediately above the lowest p-like CTTS states. We discuss how the properties of these CTTS states relate to the observed electron recombination dynamics in pump-probe experiments and then summarize all of the results of this work in Sec. IV. Finally, we include appendixes detailing the construction of our electron–THF pseudopotential and our spherical-harmonic analysis of the two-electron wave functions.

II. COMPUTATIONAL METHODS

A. Implementation of the 2EFG method in a MQC adiabatic MD algorithm

In this section, we discuss the details of how we incorporate our Fourier-grid solution to the Schrödinger equation into an MQC MD algorithm in condensed phases. Since for the present work we restrict dynamics to the electronic ground state, we assume that the Born–Oppenheimer approximation is valid. Thus, we begin by calculating the adiabatic eigenstates of the quantum degrees of freedom (in this case, the states of the two valence electrons of Na^-) at a given MD time step by solving the time-independent Schrödinger equation,

$$\hat{H}|\Psi\rangle = (\hat{h}_1 + \hat{h}_2 + \hat{r}_{12}^{-1})|\Psi\rangle = E|\Psi\rangle, \quad (1)$$

where $\hat{H}$ is the two-electron Hamiltonian, $\hat{h}_i = \hat{T}_i + \hat{V}_i$ is the single-electron Hamiltonian for electron i with kinetic and potential energy operators $\hat{T}_i$ and $\hat{V}_i$, respectively, and $\hat{r}_{12}^{-1}$ is the electron-electron Coulomb operator. The potential energy operator accounts for the interaction of the valence electrons with the instantaneous configuration of the classical particles (the solvent molecules and solute core) and is described by pseudopotentials (see below). In our 2EFG method,[1] $|\Psi\rangle$ is a two-electron eigenstate expanded in a six-dimensional (6D) real-space grid basis,

$$|\Psi\rangle = \sum_{i,j}^{N^6} \Psi_{i,j}|\mathbf{r}_i\mathbf{r}_j\rangle, \quad (2)$$

where $\{|\mathbf{r}_i\mathbf{r}_j\rangle\}$ is a 6D grid point basis function, $\{\Psi_{i,j}\}$ are real-valued expansion coefficients in this basis, and N is the number of grid points along a single spatial dimension. Equation (1) is solved using the implicitly restarted Lanczos method (IRLM) (Ref. 54) as implemented in PARPACK.[55]

Once the adiabatic electronic ground state is found, the forces exerted on the classical particles by the quantum electrons are evaluated with the Hellmann–Feynman theorem,

$$\mathbf{F}_i^Q = -\langle\Psi|\nabla_{\mathbf{R}_i}\hat{H}|\Psi\rangle, \quad (3)$$

where $\mathbf{F}_i^Q$ is the quantum force on classical particle i at position $\mathbf{R}_i$. We note that Eq. (3) is *exact* for our simulations because the wave function is expanded in a basis that does not functionally depend on the positions of the classical particles and all of the wave function expansion coefficients are variationally optimized. This represents another advantage over using atom-centered basis functions, which would necessitate adding costly Pulay force corrections to Eq. (3).[56] Using both the quantum force (evaluated from Eq. (3)) and classical forces (evaluated from the classical interaction model), the classical positions and velocities are propagated forward one MD time step. With the updated particle positions and therefore new potential energy operator, Eq. (1) is then solved for the new electronic ground state. To aid convergence, the wave function of the previous time step is used as the initial guess in the IRLM when solving for the new electronic state.

B. A new electron–THF pseudopotential

As mentioned above, we assume that the interaction of sodide's valence electrons with the solvent can be described with a pseudopotential. We recently developed a scheme based on Philips–Kleinman (PK) theory[57] that generates rigorous electron-molecule pseudopotentials,[58] and we used this scheme to derive an electron–THF pseudopotential.[59] However, this potential contained sharply varying features near THF's atomic cores (see Fig. 2 in Ref. 59), which rendered it unsuitable for use in molecular simulation because a very dense grid or other fine basis set would be needed to describe wave functions that sample the sharply varying features of this pseudopotential. Thus, to make our pseudopotential practical for condensed-phase simulation, we removed the high frequency components of our previously calculated PK pseudopotential[59] with the smoothing and fitting procedure described in Appendix A. Although the smoothing procedure means that the potential we use is no longer strictly a PK pseudopotential, the smoothed potential is identical to the original PK electron–THF pseudopotential outside of the molecular core region, where we expect most of the excess electron density to reside. The exact functional form of our new smoothed pseudopotential can be found below in Table III.

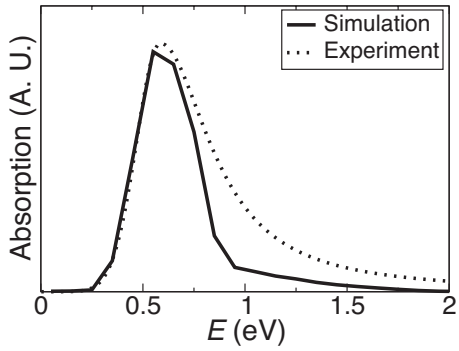

FIG. 1. Absorption spectrum of the solvated electron in liquid THF calculated from a simulation using our smoothed PK e^--THF pseudopotential via Eq. (4) with a 0.1 eV bin width (solid black curve) and taken from a Gaussian-Lorentzian fit to the experimental absorption spectrum (Ref. 60, dotted curve).

To test our smoothed PK THF pseudopotential on a real condensed-phase problem, we simulated the electronic properties (and thus the absorption spectrum) of an excess electron in liquid THF (e^-/THF), a system that we previously studied in a MQC scheme using an empirical model electron–THF potential.[49] The details of our e^-/THF simulation are the same as those in Ref. 49 with two exceptions: the model e^--THF potential was replaced with our new smoothed THF pseudopotential, and the lowest 50 adiabatic electronic states were solved with a single-electron Fourier-grid method with 32^3 grid points. We calculated the absorption spectrum of e^-/THF in the inhomogeneous broadening limit according to

$$I(E) \propto \left\langle \sum_j |\boldsymbol{\mu}_{0j}|^2 \Delta E_{0j} \delta(E - \Delta E_{0j}) \right\rangle, \quad (4)$$

where j runs over the adiabatic excited states and ΔE_{0j} and $\boldsymbol{\mu}_{0j}$ are respectively the energy difference and transition dipole between the ground and jth state. We calculated $I(E)$ using Eq. (4) with a histogram bin width of 0.1 eV and ensemble averaging over a 50 ps ground-state trajectory.

Figure 1 shows both the absorption spectrum of e^-/THF calculated from a simulation using our new smoothed PK pseudopotential (solid curve) and the experimentally measured spectrum (dotted curve). The shape of the experimental spectrum is similar to that of electrons in other solvents and is characterized by a Gaussian shape to the red of the absorption band maximum and a Lorentzian shape of the blue spectral tail.[60] The use of our new pseudopotential produces outstanding agreement of the calculated absorption spectrum with experiment: the position of the red edge of the spectrum, the spectral maximum, and the width of the peak are in

quantitative agreement. The only mild discrepancy occurs at higher energies, where the amplitude of the blue tail is somewhat underestimated in our simulation. This type of an underestimate of the blue part of the spectral tail is a problem common to MQC simulations of solvated electrons.[61–63] In light of this, we view our simulated spectrum as having outstanding agreement with experiment, thus validating the use of our smoothed PK e^--THF pseudopotential.

Although the spectrum of the solvated electron calculated with our new smoothed PK pseudopotential is in much better agreement with experiment than that calculated with our previous model potential, we note that the physical nature of the solvated electron species is similar in both sets of calculations.[49] Both sets of calculations give a solvated electron that occupies a roughly spherical solvent cavity and an absorption spectrum that arises mainly from transitions to low-lying *p*-like excited states. At higher energies, the electronic states in both calculations correspond to disjoint states supported by the naturally occurring solvent cavities.[49] The main deficiency of our previous model potential appears to be that it is overly repulsive: the radius of gyration of the solvated electron is 4.21 and 2.85 Å from the new smoothed pseudopotential and previous model potential calculations, respectively, which is presumably the origin of the significant blueshift when the spectrum was calculated using our older model potential.[49]

C. Details of the Na^-/THF simulation

To study the electronic excited states of Na^-/THF, we first generated an 80 ps equilibrium trajectory with MQC dynamics propagated on Na^-'s ground electronic state. The simulation comprised 255 classical THF molecules, one classical sodium cation core, and the two quantum mechanical valence electrons of Na^-, which were treated with our 2EFG method. The details of the classical potentials that we used have been described elsewhere.[64] Briefly, the THF molecules were treated as rigid, planar five membered rings with classical interactions that were taken from the Optimized Potential for Liquid Simulation (OPLS) model.[65,66] Periodic boundary conditions were implemented with the minimum image convention,[67] and interactions were tapered smoothly to zero at 16 Å over a 2 Å range with a center-of-mass Steinhauser switching function.[68] Dynamics was propagated in the microcanonical ensemble using the position Verlet algorithm with a time-step of 4 fs.[67] We started with a solvent configuration for a classical Na^- solute,[64] and after changing to the quantum Na^- solute, we equilibrated for 20 ps with velocity rescaling such that the average temperature in the subsequent 80 ps production run was 295 K.

The interactions between the electrons and the classical particles were treated with a PK electron–sodium cation pseudopotential[45] and the smoothed PK electron–THF pseudopotential described above and in Appendix A. The ground-state electronic wave function of sodide was represented on a 6D grid of $N=16$ points per dimension. Since this wave function was localized to the sodium core, we set the quantum grid to span only half of the 32.5 Å simulation cell length; during the simulation, particle positions were shifted every 200 fs to recenter the wave function in a manner described elsewhere.[45] By reducing the size of the quantum grid in this way, the grid density was sufficiently high that we did not need to use the aliasing correction scheme outlined in the Appendix of Paper I. For excited-state calculations, we extracted 64 statistically independent solute-solvent configurations from the 80 ps equilibrium run, each separated by 1.2 ps. For each of these configurations we then ran single point calculations to find the lowest 20 electronic adiabatic states. In order to accurately capture the diffuseness of the excited states, we set the quantum grid to span the entire simulation cell. We found it necessary to include aliasing corrections for these calculations (see the Appendix of Paper I), and from convergence checks we determined that a wave function grid with $N=28$ and an electron density grid with $N_d=48$ was necessary to achieve convergence of 0.01 eV in the excited-state eigenvalues.

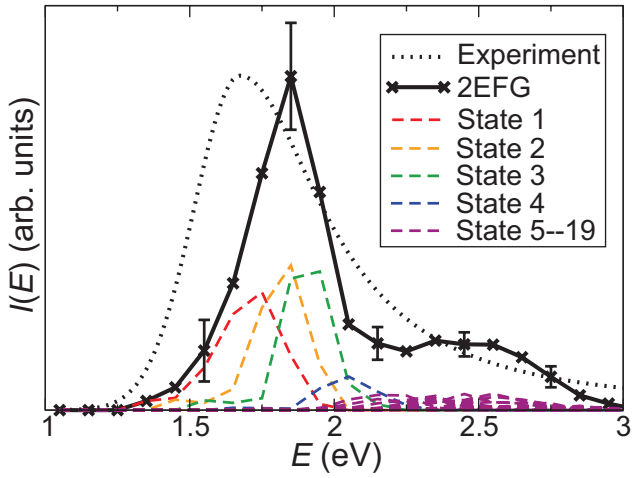

FIG. 2. Absorption spectrum of Na^-/THF both calculated from our 2EFG simulations via Eq. (4) with a 0.1 eV bin width solid curve [each bin indicated by the × symbol, with (95% confidence) error bars for the total spectrum shown at a selection of energies] and taken from a Gaussian-Lorentzian fit to the experimental spectrum (Ref. 69, dotted black curve). The dashed color curves show the contributions to the calculated spectrum from each adiabatic state.

III. RESULTS AND DISCUSSION

A. The nature of Na^-/THF's electronic states and CTTS spectrum

We begin our discussion of the electronic excited states of Na^-/THF by calculating its CTTS absorption spectrum, $I(E)$, using Eq. (4) with histogram bin widths of 0.1 eV averaged over 64 independent solvent configurations. The calculated spectrum is plotted as the solid curve in Fig. 2, and the dashed curves represent contributions to the total spectrum from each adiabatic state; the dotted curve shows the Gaussian-Lorentzian fit to the experimental spectrum,[69] which has been scaled to the maximum of our calculated spectrum. Figure 2 shows that the lowest three excited states are optically bright, giving rise to the CTTS band peak at ~1.8 eV (1.67 eV experimental[69]). As we confirm below, these are solvent-supported *p*-like CTTS states, in general agreement with experimental interpretations.[33,46,47] The width in the simulated absorption spectrum (FWHM

~0.3 eV) results mainly from a splitting of ~0.2 eV between the highest and lowest *p*-like CTTS states. Although the total simulated width is somewhat narrower than the experimental FWHM of 0.54 eV, we note the Eq. (4) neglects broadening due to the finite lifetime of the CTTS states, which based on experimental measurements[34] should provide an additional ~0.1 eV of width to Na^-/THF's spectrum. We thus consider the simulated spectrum as having good agreement with experiment, giving us confidence that our simulation model faithfully captures the electronic properties of Na^-/THF.

In addition to the three optically bright states, Fig. 2 shows that the blue tail of the Na^-/THF spectrum results from the presence of many higher-lying excited states; each of these states carries a low oscillator strength, and there is significant spectral overlap between their subbands.[70] To understand the nature of these high-lying Na^-/THF excited states, we found it clearest to visualize the difference between the excited-state charge densities and the ground-state charge density. These difference densities show where charge moves upon excitation from the ground state, revealing otherwise hard-to-see features in the shape of the excited states. Figure 3(a) presents the ground-state (labeled state 0) charge density of Na^-/THF for a representative MD configuration; the sodium cation core is shown as a black sphere with the Na^+ ionic radius of 1.1 Å, and the charge density is plotted at two contour levels: one enclosing 50% of the total charge (translucent dark blue surface) and one enclosing 90% of the total charge (transparent light blue surface). Also displayed are the locations of the closest two solvation shells of THF molecules (defined as having their centers of mass within 11.5 Å of the sodium core). As expected, Fig. 3(a) shows that the ground-state charge density is roughly spherical and is largely contained by the first solvation shell.

Panels (b)–(e) of Fig. 3 show the positive parts of the difference density between the ground state and representative excited states for the same solvent configuration shown in panel (a); in each of these panels, we have removed the solvent molecules for clarity. The translucent dark blue surfaces plot the difference densities at two different contour levels: one that encompasses the largest 0.6 *e* of the difference density (left, chosen to give the best picture of the overall shape of the excited state) and one that encompasses the largest 0.1 *e* of the difference density (right, chosen to show where charge density is most concentrated in the excited state). Panel (b) shows the difference density between the ground state and the lowest excited state (state 1); this state clearly has *p*-like symmetry. A similar analysis shows that states 2 and 3 are also *p*-like (not shown) and that these three *p*-like states are roughly orthogonally oriented. Thus, our simulations support the experimental assignment of the CTTS absorption band as arising from transitions to three orthogonally polarized *p*-like excited states.[33,46,47]

Perhaps more interestingly, Fig. 3 shows that the higher-lying excited states also appear to have significant spherical harmonic character, with state 4 [panel (c)] having a roughly spherical charge density and state 5 [panel (d)] having four lobes of charge. States 6–9 (not shown) are similar in character to state 5. This overall picture of a spherical ground state, 3 *p*-like excited states, a spherical state 4, and *d*-like states 5–9 holds for most of the MD snapshots that we analyzed, although occasionally we see configurations in which the lowest four excited states have mixed *s*- and *p*-like character. States 10 and higher are highly diffuse and have their electron density spread throughout most of the simulation box; an example of this is state 19, which is shown in Fig. 3(e). However, even these higher-lying states have significant angular variation, with state 19 having six identifiable lobes of charge density.

To better characterize the angular nature of Na^-/THF's electronic states, we projected them onto the spherical harmonics (SH). For two-electron systems such as sodide, the most relevant projection is onto products of the SHs to give the joint probability of finding one electron in angular momentum state l and the other in state l'.[45] The way we calculate our 6D SH projections is presented in Appendix B.[71] The average SH projections for the ground and 12 lowest excited states are given in Table I along with their average vertical binding energies (VBEs), defined as the difference between the instantaneous energy of Na^- and a ground-state Na^0 atom without rearrangement of the solvent.[72] Confirming what is seen in Fig. 3, Table I shows that the ground state is roughly spherically symmetric, with 85% *ss* character, and the lowest three excited states each have ~70% *sp* character. Table I also reveals that electron correlation is non-negligible, with ~8% doubly excited *pp* character in even the ground state. State 4's highest projection is on to *ss*, and states 5–9 have maximal projection onto *sd*, explaining the four lobes of charge seen in Fig. 3(c). The six lobes of charge for state 19 seen in Fig. 3(d) suggest that this state has higher angular momentum character than *d*. Therefore, for a few solvent configurations we calculated projections including the *f* SH and found that state 19, shown in Fig. 3(d), has an *sf* projection of ~55%. Similar magnitudes of *sf* projection were also seen for states 13–18, although the small energy gap between these states and higher states leads to significantly more mixing in their angular character compared to the lower CTTS states.

B. The origin of Na^-/THF's CTTS excited states

In the previous section, our simulations revealed that Na^-/THF's CTTS states actually make up a Rydberg-like series, suggesting that the CTTS electron experiences an underlying spherical confining potential around the anion. Is this spherical symmetry a result of the confinement by the first solvation shell molecules or are longer-ranged interactions important? To answer this, we calculated properties of the ground and lowest CTTS states of Na^-/THF for several independent solvent configurations and turned off different terms in the e^-−THF pseudopotential to understand which of these terms was dominant in binding the CTTS electron. According to Eq. (A3), the electron–THF pseudopotential is a sum of three terms: a short-ranged (SR) term including exchange, Pauli and tapered electrostatic potentials, $U_{SR} = U_{fit}(1-t)$, where t is a tapering function; a long-ranged Coulombic term, $U_{Coul} \times t$; and a polarization term, U_{pol}. Contributions to U_{SR} from molecules in the second solvation

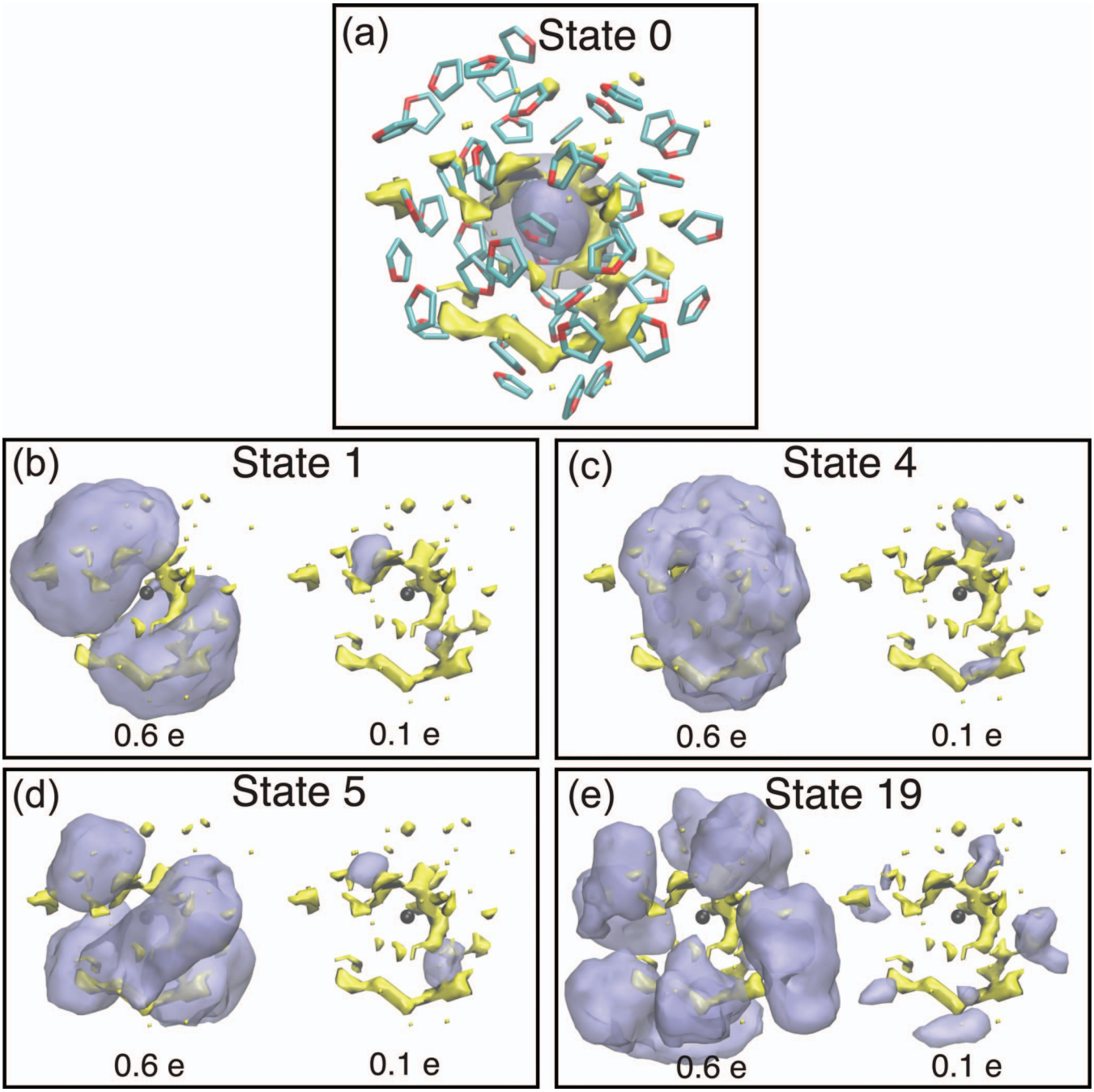

FIG. 3. Charge densities for the ground and excited states of the sodium anion in THF from a representative 2EFG MD snapshot. Panel (a) shows the two-electron ground-state charge density at two contour levels: the translucent dark blue surface encloses 50% of the charge density and the transparent lighter blue surface encloses 90%. The first solvation shell THF molecules are plotted as sticks, and the sodium cation core is shown as a black sphere with its ionic radius. Panels (b) through (e) show density differences between the ground state and excited states 1, 4, 5, and 19 at two contours: one enclosing 0.6 e of positive difference density (left image in each panel) and one enclosing 0.1 e of positive difference density (right image in each panel). Also plotted with each image are the locations of the instantaneous naturally occurring solvent voids for this configuration; the yellow surfaces enclose points that are more than 2.5 Å from any site on any solvent molecule and have an electrostatic potential that is favorable to solvate a negatively charged object. For clarity, we excluded the large solvent cavity around the Na^- anion by only plotting the yellow surface at distances greater than 3.5 Å from the sodium nucleus.

shell and further are negligible, so including only this term effectively models the confinement of Na^-'s valence electrons due to the first solvation shell molecules. In contrast, both the Coulomb and polarization terms are long-ranged interactions and therefore have contributions from all of the THF solvent molecules in the simulation.

The effects of turning off different terms in the e^--THF pseudopotential are summarized in Table II for a representative solvent configuration. The table shows that when only the SR potential (U_{SR}) is operative, the energy of the anion is actually destabilized by 0.06 eV relative to the gas phase and the lowest CTTS state is unbound (the ground-to-first-excited-state energy gap, ΔE_{01}, is larger in magnitude than the ground-state VBE). The large radius of gyration, $R_{gyr}=\langle\Psi|r^2|\Psi\rangle^{0.5}$, indicates that the unbound CTTS excited state is better thought of as a diffuse resonance. Including the somewhat longer-ranged polarization term in the potential

TABLE I. Spherical harmonic projections of the $2-e^-$ sodide wave functions, calculated using Eq. (B6) and averaged over 64 solvent configurations from an 80 ps trajectory. Projections onto *pd* and *dd* SH were calculated but are not shown since they were less than 7% for all states. The largest mean projection for each state is shown in bold.

State	VBE (eV)[a]	P_{ss}	P_{sp}	P_{sd}	P_{pp}
0	−2.98	**85**	2.8	5.2	7.9
1	−1.29	7.3	**69**	7.7	2.2
2	−1.18	5.0	**70**	8.0	2.3
3	−1.09	5.1	**68**	8.4	2.4
4	−0.95	**46**	19	22	2.7
5	−0.82	7.9	12	**54**	5.1
6	−0.76	5.8	12	**55**	4.9
7	−0.71	4.4	12	**55**	5.1
8	−0.65	3.3	16	**52**	4.6
9	−0.60	4.0	19	**48**	4.8
10	−0.54	4.8	**41**	29	4.1
11	−0.49	4.8	**45**	24	3.9
12	−0.44	5.0	**38**	22	3.4

[a]Mean Vertical Binding Energy (VBE), defined as the difference between the instantaneous energy of Na^- and a ground-state Na^0 without rearrangement of the solvent. We evaluated the energy of Na^0 using a single-electron Fourier-grid method (Ref. 49) with identical simulation parameters as presented in Sec. II C.

$(U_{SR}+U_{pol})$ stabilizes the ground-state anion by ~1 eV and causes the first-excited state to be bound; however, the other properties of the electronic states, such as the energy gap and radial extent, are largely unchanged from the SR calculation. Table II also shows that the Coulomb terms are the most important part of the e^--THF pseudopotential since adding them to $U_{SR}+U_{pol}$ to yield the full pseudopotential (U_{total}) adds an additional ~1.5 eV of stabilization to the ground state. The Coulomb potential also compresses the excited-state wave functions and opens up the ground-to-excited-state energy gap to produce better agreement with experiment. Thus, it is the long-ranged polarization of the solvent that causes the anion's CTTS excited states to be bound. This agrees with Bradforth and Jungwirth's finding that long-range solvent polarization is also the dominant mechanism stabilizing the CTTS excited state of I^-/H_2O.[43]

The long-range polarization of THF around Na^- is therefore the origin of the underlying spherically symmetric confining potential that gives rise to the Rydberg-like series of bound CTTS states. Figure 3 and Table I make it clear, however, that Na^-/THF's CTTS states are also sensitive to the local details of the solvent packing. This is most clearly seen in the 0.1 *e* contours at the right of panels (b)–(e) of Fig. 3, which show where charge density is most concentrated for excited states 1, 4, 5, and 19. At this contour level, the spherical-harmonic character of the states is no longer recognizable; instead, we see that charge density is mostly localized in only a few regions of space. What determines the locations of these regions of high excited-state charge density? The yellow surface in Fig. 3 shows, for this particular solvent configuration, the location of the voids that naturally occur in liquid THF: the yellow surface marks regions of

TABLE II. Dependence of electronic properties of sodide on different terms in the electron–THF pseudopotential. The numbers shown here are for a representative snapshot. The values for other snapshots differ, but the trends are robust.

System	VBE (eV)[a]	ΔE_{01} (eV)[b]	R_0^{gyr} (Å)[c]	R_1^{gyr} (Å)[c]
Isolated Na^- ion				
Calculation[d]	−0.539	⋯	3.37	⋯
Experiment	–0.548[80]	⋯	⋯	⋯
Condensed-phase Na^- ion				
Calculation with U_{SR} [e]	−0.479	1.05	2.76	6.64
Calculation with $U_{SR}+U_{pol}$ [f]	−1.53	1.10	2.82	6.47
Calculation with U_{total} [g]	−2.98	1.55	2.66	4.60
Experiment	⋯	1.59[46]	3.4[29]	⋯

[a]VBE, as defined in Table I.
[b]Ground-to-first-excited-state energy gap.
[c]R_i^{gyr} is the radius of gyration of the *i*th-state charge density.
[d]The simulation parameters for the isolated ion calculation are identical to the condensed-phase anion simulation.
[e]Including only the SR terms in the THF pseudopotential.
[f]Including only the SR and polarization terms in the THF pseudopotential.
[g]Including all terms in the THF pseudopotential.

space that are ≥2.5 Å from any site on any of the THF solvent molecules and for which the value of the e^--THF pseudopotential is attractive to an excess electron (≤−0.065 hartree).[49] Inspection of Fig. 3 shows that the maximum charge density for each of Na^-/THF's CTTS excited states is indeed localized in the naturally occurring solvent cavities. The optically bright *p*-like states are localized in voids in the first-solvent shell, while the higher-lying states explore voids located further from the anion. We saw this behavior in every snapshot we examined. Thus, even though the Rydberg-like series of Na^-/THF CTTS states is bound by the long-range solvent polarization, the presence of these solvent-bound excited states is also supported by the naturally occurring voids in the liquid.

C. The relation between Na^-/THF CTTS electronic structure and electron ejection and recombination dynamics

One of the interesting experimental features observed for CTTS reactions in liquid THF and other ethers is that following photoexcitation, the ejected solvated electrons appear after a ~0.5 ps time delay, and they do so with their equilibrium absorption spectrum.[7,26,27,31,46] This behavior is in sharp contrast to the CTTS dynamics of iodide observed in water and alcohols, where essentially instantaneous electron ejection is followed by slower solvation of the electron on picosecond time scales.[3,6,10,11,14–16] In this section, we show that these differences in CTTS behavior in liquid THF and ethers versus other solvents can be understood in light of the properties of the CTTS states revealed in Fig. 3. The unusual electron ejection dynamics in THF and other ethers results from the fact that CTTS photoexcitation populates states in which the excited electron is initially delocalized over multiple solvent voids, as seen directly in Fig. 3. In this respect, the excited states of Na^- match the excited states of the solvated electron in THF seen in previous simulations.[49,50] These simulations found that solvent motions subsequent to the excitation cause the excited electron to localize into one of the voids on a ~0.5 ps time scale via a nonadiabatic transition.[50] Because the solvent surrounding the voids is already favorably arranged to solvate an electron,[49,51] the ejected electron from Na^- thus equilibrates with the solvent on a time scale faster than it is localized, creating a situation where the electron appears with its equilibrium spectrum even though its appearance is delayed.[26,27,29,31]

Another interesting feature of the Na^-/THF CTTS reactions is the fact that the recombination dynamics of the ejected CTTS electrons depends strongly on the excitation wavelength. When sodide is photoexcited on the red side of its CTTS absorption peak, virtually all the ejected electrons recombine with Na^0 on a ~1 ps time scale, whereas excitation on the high-energy side of the CTTS band leads to populations of electrons that recombine on ~200 ps and ≥ns time scales.[21] This behavior was interpreted as correlating with the distance the electron was ejected from the sodium nucleus: red-edge excitation was argued as ejecting electrons into the same solvent cage as their geminate sodium atom partners (forming so-called "immediate" contact pairs that recombine quickly), while higher-energy excitation ejected

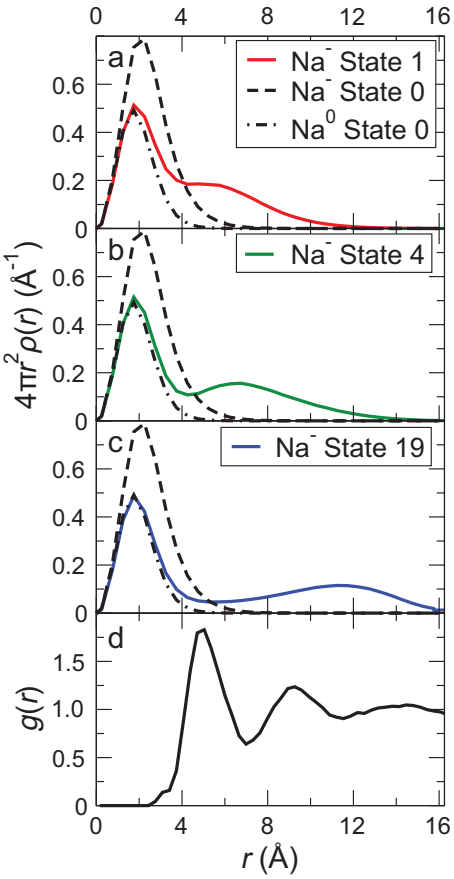

FIG. 4. Spherically averaged radial densities for the ground and excited states of Na^-/THF. In panels (a)–(c) we plot the excited-state radial densities of Na^- as solid color curves. Panel (a): state 1 (red). Panel (b): state 4 (green). Panel (c): state 19 (blue). Also plotted in each panel are the radial densities for the ground state of Na^- (dashed black curve) and the ground state of Na^0 in the same solvent configuration (dot-dashed black curve). For comparison, we plot the RDF, $g(r)$, for the Na^+ core–THF center of mass distances in panel (d).

electrons either one solvent shell away from the sodium atom (forming "solvent-separated" contact pairs that recombine in hundreds of ps) or even further out into the liquid (forming 'free' electrons that recombine on diffusive time scales).[21] These ideas are reinforced by our simulations: Fig. 3 shows that the majority of the electron density of the CTTS states of Na^-/THF lies in the naturally occurring solvent voids, with higher-energy CTTS states in voids that lie farther from the anion. Thus, our simulations suggest that the three different time scales for recombination observed in the experiments are a direct consequence of the radial character of the initially excited CTTS state.

In Figs. 4(a)–4(c), we explore the radial character of some of the CTTS states (colored curves) as well as the ground state (black dashed curves) of Na^-/THF by spherically averaging the electron density in radial bins of 0.5 Å width with the Na^+ core at the origin and ensemble averaging over 64 independent solvent configurations. To understand where these charge densities reside in relation to the solvent molecules, we show the radial distribution function (RDF), $g(r)$, for the Na^+ core–THF center-of-mass distances in panel (d) of Fig. 4. The RDF shows a well-defined first solvation peak at 4.9 Å and two smaller peaks at 9.2 and ~14 Å

corresponding to second and third solvation shells, respectively. In the case of the first CTTS excited state [state 1, red solid curve, panel (a)], the excited-state charge density is located in solvent voids within the anion's first solvation shell; we see similar results for the other *p*-like states, 2 and 3 (not shown). These three states will be selectively populated when sodide is excited at wavelengths to the red of the CTTS band maximum, so it is reasonable to expect that the dynamics subsequent to populating one of these states involves motion of the first-solvent shell molecules to solvate the detached electrons in the same solvent cage as their Na^0 partners, in accord with experiment. For state 4, plotted as the green solid curve in panel (b), the excited electron density builds up in between the first and second solvation shells, and a similar profile is seen in states 5–10 (not shown). These are the states that will be populated upon photoexcitation to the blue of the CTTS band maximum, and the expectation that these electrons ultimately localize one solvent shell away from their Na^0 atom partners is in qualitative agreement with the experimental observation of solvent-separated electrons being generated at these excitation wavelengths. Finally, for our higher calculated states (11–19), illustrated by state 19 in panel (c), the electron density fills most of the simulation cell (16.25 Å represents half the cell length), peaking between the second and third solvation shells. Excitation to one of these states is therefore likely to generate a free electron, again in accord with experiment.

In addition to providing a rationale for the change in recombination dynamics of the CTTS electron following photoexcitation at different wavelengths, the radial densities in Figs. 4(a)–4(c) also reveal changes in the electronic structure immediately surrounding the sodium atom core. Comparing the excited-state densities (solid color curves) to the radial density of a ground-state Na^0 atom in the solvent cavity of the anion (dot-dashed black curve), we see nearly perfect overlap: in other words, photoexcitation essentially promotes one of the two valence electrons to the CTTS excited state and leaves the other in what is essentially the ground state of the neutral sodium atom. This agrees with pump-probe experiments on Na^-/THF, which find that the transient absorption corresponding to Na^0 appears with an instrument-limited rise following photoexcitation,[7,19,26,32,33,46] even with ~15 fs time resolution.[34] Thus, even though a proper treatment of exchange and correlation is critical for determining CTTS energetics and the local solvent structure,[43,45] our results indicate that for Na^-/THF, CTTS excitation is essentially a one-electron transition.

IV. CONCLUSIONS

In this paper we applied our recently developed 2EFG simulation method to study the CTTS states of Na^-/THF. Our method, which explicitly solves for the wave function of Na^-'s two valence electrons in a 6D grid basis, provides an accurate treatment of electron correlation and is also able to describe the highly diffuse electronic excited states that reside far from any atomic centers. Our simulations confirm previous experimental assignments of the peak in sodide's absorption spectrum as arising from three *p*-like CTTS states;[21,33,47] however, we find that these *p* states lie at the bottom of a Rydberg-like progression with higher-lying CTTS states of *s*-, *p*-, *d*-, and even *f*-like angular character. These CTTS states are not just supported by the solvent polarization surrounding the ground-state sodium anion, but they are also highly mixed with the disjoint states supported by the naturally occurring solvent cavities in liquid THF. Thus, the CTTS excited states have their highest charge density located in regions of space that are devoid of solvent molecules.

The electronic structure of the CTTS states seen in our simulation explains many of the experimental observations associated with the ultrafast transient absorption dynamics of Na^-/THF. The strong mixing of the CTTS states with disjoint solvent-cavity states explains the experimental observation that localization of the ejected CTTS electrons requires a ~0.5 ps delay following photoexcitation of Na^-/THF, even though the ejected electrons appear with their equilibrium absorption spectrum.[7,26,27,31,46] This is because it takes ~0.5 ps for solvent motions to induce the nonadiabatic transition that localizes the diffuse CTTS excited state into one of the solvent cavities, but once localized, the cavity is already favorably oriented to solvate the electron so that little additional relaxation is required. In addition, the fact that higher-lying CTTS states access solvent cavities that are further from the parent anion explains the strong dependence of electron recombination dynamics on excitation wavelength in pump-probe experiments.[21] At low excitation energies, the CTTS electron is excited into cavities in the first solvation shell, leading to the formation of a rapidly recombining (Na^0:e^-) immediate contact pair. At intermediate excitation energies, the CTTS electron is mainly promoted into cavities one solvent shell away from the anion, forming a more slowly recombining (~100 ps) solvent-separated contact pair with the Na^0. At higher excitation energies, the CTTS electron is excited into cavities more than two solvent shells away, yielding free solvated electrons that recombine diffusively. Finally, our examination of the radial properties of the CTTS states reveals that the ground-state Na^0 atom is formed essentially instantly upon excitation, in agreement with what is observed in pump-probe experiments.[7,19,26,32–34,46]

In addition to explaining the features of pump-probe experiments, our simulations also were able to pinpoint which interactions of THF with Na^- are responsible for stabilizing the CTTS excited states. We found that the main source of stabilization comes from the long-range polarization of the solvent, both nuclear and electronic, induced by the presence of the sodium anion. Since solvent polarization is a universal feature to polar solvent-anion interactions, we expect that similar Rydberg progressions of CTTS excited states may exist with other solute/solvent combinations. We do not expect such progressions to occur in solvents such as water or alcohols where the conduction band lies just above the first CTTS state of the anion,[43] but they may be a universal feature in cavity-containing solvents such as ethers, where the presence of cavities can stabilize such states below the solvent conduction band. In addition, the far ultraviolet spectra of iodide in other solvents, such as organic nitriles, reveal the presence of higher-lying CTTS bands that do not exist in

water.[73] The nature of these states is as of yet unknown,[3] and it would be interesting to perform calculations at the level of our 2EFG method on these CTTS systems to better understand the solute-solvent interactions that lead to the formation of stable CTTS excited states.

ACKNOWLEDGMENTS

We gratefully acknowledge the UCLA Institute for Digital Research and Education for allocating computer time for the calculations presented in this paper. We also thank Cesar Mejia for his contribution to the development of the electron–THF pseudopotential and Art Bragg for stimulating discussions. This work was supported by the National Science Foundation under Grant Nos. CHE-0603766 and CHE-0908548 and the American Chemical Society Petroleum Research Fund under Grant No. 45988-AC,6.

APPENDIX A: SMOOTHING AND REPARAMETRIZATION OF THE ELECTRON–THF PSEUDOPOTENTIAL

This appendix describes the procedures we went through to smooth our previously derived e^--THF pseudopotential[59] for use in molecular simulation. We needed to smooth our previously derived potential because like most PK pseudopotentials, it has very sharply varying features that are hard to represent with reasonably sized basis sets in quantum chemistry calculations. The sharply varying features in PK pseudopotentials result from taking the wave function of the excess electron (the so-called pseudo-orbital $|\phi\rangle$) to be a linear combination of the molecule's core orbitals and the lowest unoccupied molecular orbital (LUMO),

$$|\phi\rangle = |\psi_v\rangle + \sum_{i=1}^{ncore} |\psi_i\rangle\langle\psi_i|\phi\rangle, \tag{A1}$$

where $|\psi_v\rangle$ is the LUMO and $|\psi_i\rangle$ is the ith core orbital, of which there are *ncore*. Following Cohen and Heine,[74] we choose the particular linear combination in Eq. (A1) that minimizes the expectation value of the kinetic-energy operator. This procedure produces a nodeless pseudo-orbital; however, sharp features still remain in the core region of the pseudo-orbital [due to the core orbitals in Eq. (A1)], which are amplified in the inversion of the one-electron Schrödinger equation when calculating the pseudopotential

$$V(\mathbf{r}) = \frac{\langle \mathbf{r}|(\epsilon - \hat{T})|\phi\rangle}{\langle \mathbf{r}|\phi\rangle}, \tag{A2}$$

where ϵ is the LUMO energy. To avoid these sharp features, we follow standard atomic pseudopotential generation schemes[75–77] and generate a smoothed pseudo-orbital to ensure that the pseudopotential from Eq. (A2) is also smooth. To do this, we convolved the kinetic-energy minimized THF pseudo-orbital from Ref. 59 with a Gaussian function with a FWHM of 1.92 bohr.[78] Using Eq. (A2), the pseudopotential was then generated on an evenly spaced grid of 64^3 points with a grid spacing of 0.3125 bohr. The resulting smoothed potential matched the full PK pseudopotential outside of the molecular core region. Inside the core region, the potential displayed the gross features of the full PK pseudopotential but without any of the sharply varying features near the atomic sites.

To make the smoothed THF pseudopotential practical for molecular simulation, we fit a 41-parameter function, $U_{\text{fit}}(\mathbf{r})$ shown in Table III, to the smoothed THF pseudopotential

TABLE III. Functional form and parameters of the fit to the smoothed PK electron–THF pseudopotential. The 41-parameter fit has functional contributions centered on 15 different sites. The functional and parameter notations are explained in Ref. 59 and the text. For the parameters given here, the distances are in bohr radii, and the energies are in hartrees.

$$U_{\text{fit}}(\mathbf{r}) = \{U_o + U_{h\alpha 1} + U_{h\alpha 2} + U_{h\alpha 3} + U_{h\alpha 4} + U_{h\beta 1} + U_{h\beta 2} + U_{h\beta 3} + U_{h\beta 4} + U_{ao1} + U_{ao2} + U_{ac1} + U_{ac2} + U_{aa} + U_{am}$$

$$U_o(\mathbf{r}-\mathbf{r_o}) = (o_1(x-x_o)^4 + o_2(y-y_o)^4 - o_3(z-z_o)^4 - o_4)\exp(-[o_5(x-x_o)^2 + o_6((y-y_o)^2 + (z-z_o)^2)])$$
$o_1 = 0.004\,040\,36$, $o_2 = 0.028\,383\,0$, $o_3 = 0.005\,898\,37$, $o_4 = 0.073\,700\,1$, $o_5 = 0.542\,837$, $o_6 = 0.234\,444$

$$U_{h\alpha}(\mathbf{r}-\mathbf{r_{h\alpha}}) = -h_1^\alpha \frac{\exp[-h_2^\alpha(\mathbf{r}-\mathbf{r}_{h\alpha})^2]}{|\mathbf{r}-\mathbf{r}_{h\alpha}| + h_3^\alpha} + h_4^\alpha \exp[-h_5^\alpha(\mathbf{r}-\mathbf{r}_{h\alpha})^2]$$
$h_1^\alpha = 1.255\,77$, $h_2^\alpha = 0.524\,964$, $h_3^\alpha = 5.114\,36$, $h_4^\alpha = 0.017\,110\,9$, $h_5^\alpha = 0.030\,270\,5$

$$U_{h\beta}(\mathbf{r}-\mathbf{r_{h\beta}}) = -h_1^\beta \frac{\exp[-h_2^\beta(\mathbf{r}-\mathbf{r}_{h\beta})^2]}{|\mathbf{r}-\mathbf{r}_{h\beta}| + h_3^\beta} + h_4^\beta \exp[-h_5^\beta(\mathbf{r}-\mathbf{r}_{h\beta})^2]$$
$h_1^\beta = 2.209\,64$, $h_2^\beta = 0.530\,891$, $h_3^\beta = 7.474\,54$, $h_4^\beta = -0.004\,650\,49$, $h_5^\beta = 0.010\,623\,7$

$$U_{ao}(\mathbf{r}-\mathbf{r_{ao}}) = a_1^o \exp[-(a_2^o(x-x_{ao})^2 + a_3^o(y-y_{ao})^2 + a_4^o(z-z_{ao})^2)]$$
$a_1^o = 0.129\,850$, $a_2^o = 0.106\,785$, $a_3^o = 0.490\,548$, $a_4^o = 0.113\,171$, $x_{ao} = 0.000\,00$, $y_{ao} = \pm 1.295\,47$, $z_{ao} = 3.496\,76$

$$U_{ac}(\mathbf{r}-\mathbf{r_{ac}}) = a_1^c \exp[-(a_2^c(x-x_{ac})^2 + a_3^c(y-y_{ac})^2 + a_4^c(z-z_{ac})^2)]$$
$a_1^c = 0.415\,117$, $a_2^c = 0.398\,365$, $a_3^c = 0.495\,326$, $a_4^c = 0.296\,150$, $x_{ac} = 0.000\,00$, $y_{ac} = \pm 3.118\,63$, $z_{ac} = -1.044\,68$

$$U_{aa}(\mathbf{r}-\mathbf{r_{aa}}) = a_1^a \exp[-(a_2^a(x-x_{aa})^2 + a_3^a(y-y_{aa})^2 + a_4^a(z-z_{aa})^2)] - a_5^a \exp[-(a_6^a(x-x_{aa})^2 + a_7^a(y-y_{aa})^2 + a_8^a(z-z_{aa})^2)]$$
$a_1^a = 11.8629$, $a_2^a = 0.213\,713$, $a_3^a = 0.067\,522\,7$, $a_4^a = 0.276\,804$, $a_5^a = 11.5334$, $a_6^a = 0.213\,048$, $a_7^a = 0.067\,017\,9$, $a_8^a = 0.277\,229$,
$x_{aa} = 0.000\,00$, $y_{aa} = 0.000\,00$, $z_{aa} = -3.415\,60$

$$U_{am}(\mathbf{r}-\mathbf{r_{am}}) = -a_1^m \exp[-(a_2^m(x-x_{am})^2 + a_3^m(y-y_{am})^2 + a_4^m(z-z_{am})^2)]$$
$a_1^m = 0.117\,890$, $a_2^m = 0.246\,939$, $a_3^m = 0.008\,836\,31$, $a_4^m = 0.250\,737$, $x_{am} = 0.000\,00$, $y_{am} = 0.000\,00$, $z_{am} = 0.000\,00$

generated on the grid. The functional form of $U_{\mathrm{fit}}(\mathbf{r})$ was taken from Ref. 59 with a few modifications: we removed the original carbon-centered terms, $U_{c\alpha}$ and $U_{c\beta}$, which we found were not needed to fit the smoothed pseudopotential, and we added a single center-of-mass site term, U_{am}, which greatly improved the quality of the fit. As described previously,[59] to ensure the correct long-range asymptotic behavior, we tapered the potential fit into THF's asymptotic Coulomb potential and also added a polarization term,

$$U_{\mathrm{total}}(\mathbf{r}) = U_{\mathrm{fit}}(\mathbf{r})(1 - t(\mathbf{r})) + U_{\mathrm{Coul}}(\mathbf{r})t(\mathbf{r}) + U_{\mathrm{pol}}(\mathbf{r}), \quad \text{(A3)}$$

where $\mathbf{r}$ is relative to the THF center-of-mass and $U_{\mathrm{Coul}}(\mathbf{r})$ is THF's Coulomb potential resulting from the Mulliken charges on the THF sites, with $q_o = -0.412\,943e$ (oxygen site), $q_{c\alpha} = +0.186\,071e$ (α methylene site), and $q_{c\beta} = +0.020\,400\,5e$ (β methylene site).[79] The tapering function is

$$t(\mathbf{r}) = \frac{1}{e^{-10((r/r_0)^2-1)} + 1}, \quad \text{(A4)}$$

with $r_0 = 8$ bohr. The polarization term was taken from Ref. 49,

$$U_{\mathrm{pol}}(\mathbf{r}) = -\sum_i^5 \frac{\alpha_i}{2|\mathbf{r} - \mathbf{r}_i|^4}(1 - e^{|\mathbf{r}-\mathbf{r}_i|/r_d})^6, \quad \text{(A5)}$$

where the sum on i runs over the five solvent sites (1 = oxygen, 2,3 = α methylene, and 4,5 = β methylene) and the site polarizabilities are $\alpha_1 = 17.5$, $\alpha_{2,3,4,5} = 7.7097$ a.u. The term in parentheses in Eq. (A5) is a damping function that prevents the polarization potential from unphysically diverging at the solvent site centers. The damping radius, r_d, originally set at 1.18 bohr in Ref. 49, was deemed to be too small given the extent of the core electrons' charge density in THF, so it was increased to $r_d = 3$ bohr. Although the polarization term is fairly *ad hoc* in nature, in a condensed-phase simulation this part of the potential is rather flat and therefore does not substantially affect the properties of electronic states apart from a slight shifting of their absolute energies.[80]

APPENDIX B: PROJECTION OF 6D WAVE FUNCTIONS ONTO SPHERICAL HARMONICS

In this appendix, we derive the equations used to project 6D grid-based wave functions onto products of SH. The derivation is an extension of the method of Sheu and Rossky for three-dimensional grid-based wave functions.[38] We start by expanding the 6D wave function, $\Psi(\mathbf{r}_1, \mathbf{r}_2)$, in terms of SH,

$$\Psi(\mathbf{r}_1, \mathbf{r}_2) = \sum_{l,m} \sum_{l',m'} \mathcal{R}_{l,m,l',m'}(r_1, r_2) Y_{l,m}(\Omega_1) Y_{l',m'}(\Omega_2), \quad \text{(B1)}$$

where $Y_{l,m}(\Omega_{1(2)})$ is a SH in electron 1(2)'s angular coordinates and $\mathcal{R}_{l,m,l',m'}$ is the expansion coefficient,

$$\mathcal{R}_{l,m,l',m'}(r_1, r_2) = \int d\Omega_1 \int d\Omega_2 \Psi(\mathbf{r}_1, \mathbf{r}_2) \times Y^*_{l,m}(\Omega_1) Y^*_{l',m'}(\Omega_2), \quad \text{(B2)}$$

and $\Omega_{1(2)}$ is the solid angle for electron 1(2). The probability $P_{l,m,l',m'}$ to find electron 1 in angular momentum state $|l,m\rangle$ while electron 2 is in angular momentum state $|l',m'\rangle$ is then given by the square modulus of $\mathcal{R}_{l,m,l',m'}(r_1, r_2)$, integrated over the radial coordinates r_1 and r_2,

$$P_{l,m,l',m'} = \int dr_1 r_1^2 \int dr_2 r_2^2 |\mathcal{R}_{l,m,l',m'}(r_1, r_2)|^2. \quad \text{(B3)}$$

In principle, all we need to do is calculate $\mathcal{R}_{l,m,l',m'}(r_1, r_2)$ using Eq. (B2) for the desired combinations of l, m, l' and m' and use these values in Eq. (B3) to find the projections that we seek.

Evaluating Eq. (B2) is problematic, however, because $\Psi(\mathbf{r}_1, \mathbf{r}_2)$ is represented on a 6D Cartesian grid, and transforming to polar coordinates would involve fitting the wave function between grid points. Thus, we follow Sheu and Rossky[38] and manipulate Eq. (B3) to allow all of the integrals to be done on the Cartesian grid. The trick is to introduce additional radial integrals with delta functions,

$$P_{l,m,l',m'} = \int dr_1 r_1 \int dr_1' r_1' \int dr_2 r_2 \int dr_2' r_2' \times \mathcal{R}_{l,m,l',m'}(r_1, r_2) \times \mathcal{R}^*_{l,m,l',m'}(r_1', r_2') \delta(r_1 - r_1') \times \delta(r_2 - r_2'). \quad \text{(B4)}$$

After substituting Eq. (B2) into Eq. (B4), using the Fourier representation of the delta function,

$$\delta(r - r') = (1/2\pi) \int_{-\infty}^{\infty} dk e^{ik(r-r')}, \quad \text{(B5)}$$

and manipulating, we obtain our final expression,

$$P_{l,m,l',m'} = \frac{1}{\pi^2} \int_0^\infty dk_1 \int_0^\infty dk_2 \left| \int d^3\mathbf{r}_1 \int d^3\mathbf{r}_2 \Psi(\mathbf{r}_1, \mathbf{r}_2) Y^*_{l,m}(\Omega_1) Y^*_{l',m'}(\Omega_2) \frac{\cos(k_1 r_1)\cos(k_2 r_2)}{r_1 r_2} \right|^2 + \left| \int d^3\mathbf{r}_1 \int d^3\mathbf{r}_2 \Psi(\mathbf{r}_1, \mathbf{r}_2) Y^*_{l,m}(\Omega_1) Y^*_{l',m'}(\Omega_2) \frac{\cos(k_1 r_1)\sin(k_2 r_2)}{r_1 r_2} \right|^2 + \left| \int d^3\mathbf{r}_1 \int d^3\mathbf{r}_2 \Psi(\mathbf{r}_1, \mathbf{r}_2) Y^*_{l,m}(\Omega_1) Y^*_{l',m'}(\Omega_2) \frac{\sin(k_1 r_1)\cos(k_2 r_2)}{r_1 r_2} \right|^2 + \left| \int d^3\mathbf{r}_1 \int d^3\mathbf{r}_2 \Psi(\mathbf{r}_1, \mathbf{r}_2) Y^*_{l,m}(\Omega_1) Y^*_{l',m'}(\Omega_2) \frac{\sin(k_1 r_1)\sin(k_2 r_2)}{r_1 r_2} \right|^2. \quad \text{(B6)}$$

Thus, all the spatial integrals (over $\mathbf{r}_1$ and $\mathbf{r}_2$) in Eq. (B6) are now in Cartesian coordinates and can be simply evaluated on the real-space grid on which the wave function is stored. The price paid for this convenience is that Eq. (B6) contains two k integrals, which we evaluated using Simpson's rule with 9 quadrature points from $k=0$ up to the largest k the grid supports: $k_{\max}=\pi/(2a)$, where a is the grid spacing. Evaluating Eq. (B6) thus involves $9^2\times 4=324$ 6D integrals for every unique choice of l,m,l' and m' and is thus computationally demanding [although this calculation is fairly easy to parallelize since $\Psi(\mathbf{r}_1,\mathbf{r}_2)$ is the only 6D function in the integrand and it is already distributed over all the CPUs in the calculation, as described in Paper I]. Finally, in order the calculate the probability of finding one electron in angular momentum state l while the other is in state l', we add $P_{l,m,l',m'}$ and $P_{l',m',l,m}$ and sum over m and m'.

[1] W. J. Glover, R. E. Larsen, and B. J. Schwartz, J. Chem. Phys. **132**, 144101 (2010).
[2] M. J. Blandamer and M. F. Fox, Chem. Rev. (Washington, D.C.) **70**, 59 (1970).
[3] X. Chen and S. E. Bradforth, Annu. Rev. Phys. Chem. **59**, 203 (2008).
[4] J. Jortner, M. Ottolenghi, and G. Stein, J. Phys. Chem. **68**, 247 (1964).
[5] Y. Gauduel, H. Gelabert, and M. Ashokkumar, Chem. Phys. **197**, 167 (1995).
[6] J. A. Kloepfer, V. H. Vilchiz, V. A. Lenchenkov, and S. E. Bradforth, Chem. Phys. Lett. **298**, 120 (1998).
[7] E. R. Barthel, I. Martini, and B. J. Schwartz, J. Chem. Phys. **112**, 9433 (2000).
[8] F. H. Long, H. Lu, X. Shi, and K. B. Eisenthal, Chem. Phys. Lett. **169**, 165 (1990).
[9] F. H. Long, X. L. Shi, H. Lu, and K. B. Eisenthal, J. Phys. Chem. **98**, 7252 (1994).
[10] J. A. Kloepfer, V. H. Vilchiz, V. A. Lenchenkov, A. C. Germaine, and S. E. Bradforth, J. Chem. Phys. **113**, 6288 (2000).
[11] V. H. Vilchiz, J. A. Kloepfer, A. C. Germaine, V. A. Lenchenkov, and S. E. Bradforth, J. Phys. Chem. A **105**, 1711 (2001).
[12] J. A. Kloepfer, V. H. Vilchiz, V. A. Lenchenkov, X. Y. Chen, and S. E. Bradforth, J. Chem. Phys. **117**, 766 (2002).
[13] M. C. Sauer, I. A. Shkrob, R. Lian, R. A. Crowell, D. M. Bartels, X. Y. Chen, D. Suffern, and S. E. Bradforth, J. Phys. Chem. A **108**, 10414 (2004).
[14] V. H. Vilchiz, X. Chen, J. A. Kloepfer, and S. E. Bradforth, Radiat. Phys. Chem. **72**, 159 (2005).
[15] R. Lian, D. A. Oulianov, R. A. Crowell, I. A. Shkrob, X. Y. Chen, and S. E. Bradforth, J. Phys. Chem. A **110**, 9071 (2006).
[16] A. C. Moskun, S. E. Bradforth, J. Thogersen, and S. Keiding, J. Phys. Chem. A **110**, 10947 (2006).
[17] M. C. Sauer, R. A. Crowell, and I. A. Shkrob, J. Phys. Chem. A **108**, 5490 (2004).
[18] I. B. Martini, E. R. Barthel, and B. J. Schwartz, J. Chem. Phys. **113**, 11245 (2000).
[19] E. R. Barthel, I. Martini, and B. J. Schwartz, J. Phys. Chem. B **105**, 12230 (2001).
[20] I. B. Martini, E. R. Barthel, and B. J. Schwartz, J. Am. Chem. Soc. **124**, 7622 (2002).
[21] E. R. Barthel and B. J. Schwartz, Chem. Phys. Lett. **375**, 435 (2003).
[22] E. R. Barthel, I. B. Martini, E. Keszei, and B. J. Schwartz, in *Ultrafast Phenomena XIII*, edited by M. Murnane, N. Scherer, R. J. D. Miller, and A. M. Weiner (Springer-Verlag, Berlin, 2003), pp. 459–461.
[23] I. B. Martini, E. R. Barthel, and B. J. Schwartz, in *Ultrafast Phenomena XIII*, edited by M. Murnane, N. Scherer, R. J. D. Miller, and A. M. Weiner (Springer-Verlag, Berlin, 2003), pp. 487–489.
[24] I. B. Martini and B. J. Schwartz, J. Chem. Phys. **121**, 374 (2004).
[25] I. B. Martini, E. R. Barthel, and B. J. Schwartz, Pure Appl. Chem. **76**, 1809 (2004).
[26] M. C. Cavanagh, R. E. Larsen, and B. J. Schwartz, J. Phys. Chem. A **111**, 5144 (2007).
[27] A. E. Bragg and B. J. Schwartz, J. Phys. Chem. B **112**, 483 (2008).
[28] A. E. Bragg and B. J. Schwartz, J. Phys. Chem. A **112**, 3530 (2008).
[29] M. C. Cavanagh, R. M. Young, and B. J. Schwartz, J. Chem. Phys. **129**, 134503 (2008).
[30] A. E. Bragg, M. C. Cavanagh, and B. J. Schwartz, Science **321**, 1817 (2008).
[31] M. C. Larsen and B. J. Schwartz, J. Chem. Phys. **131**, 154506 (2009).
[32] Z. H. Wang, O. Shoshana, B. X. Hou, and S. Ruhman, J. Phys. Chem. A **107**, 3009 (2003).
[33] O. Shoshana, J. L. P. Lustres, N. P. Ernsting, and S. Ruhman, Phys. Chem. Chem. Phys. **8**, 2599 (2006).
[34] O. Shoshanim and S. Ruhman, J. Chem. Phys. **129**, 044502 (2008).
[35] W. S. Sheu and P. J. Rossky, Chem. Phys. Lett. **202**, 186 (1993).
[36] W. S. Sheu and P. J. Rossky, Chem. Phys. Lett. **213**, 233 (1993).
[37] W. S. Sheu and P. J. Rossky, J. Am. Chem. Soc. **115**, 7729 (1993).
[38] W. S. Sheu and P. J. Rossky, J. Phys. Chem. **100**, 1295 (1996).
[39] D. Borgis and A. Staib, Chem. Phys. Lett. **230**, 405 (1994).
[40] A. Staib and D. Borgis, J. Chem. Phys. **104**, 9027 (1996).
[41] D. Borgis and A. Staib, J. Chem. Phys. **104**, 4776 (1996).
[42] D. Borgis and A. Staib, J. Phys.: Condens. Matter **8**, 9389 (1996).
[43] S. E. Bradforth and P. Jungwirth, J. Phys. Chem. A **106**, 1286 (2002).
[44] C. J. Smallwood, W. B. Bosma, R. E. Larsen, and B. J. Schwartz, J. Chem. Phys. **119**, 11263 (2003).
[45] W. J. Glover, R. E. Larsen, and B. J. Schwartz, J. Chem. Phys. **129**, 164505 (2008).
[46] E. R. Barthel, I. B. Martini, E. Keszei, and B. J. Schwartz, J. Chem. Phys. **118**, 5916 (2003).
[47] J. L. Dye and M. G. DeBacker, Annu. Rev. Phys. Chem. **38**, 271 (1987).
[48] W. J. Glover, R. E. Larsen, and B. J. Schwartz, (2010) (unpublished).
[49] M. J. Bedard-Hearn, R. E. Larsen, and B. J. Schwartz, J. Chem. Phys. **122**, 134506 (2005).
[50] M. J. Bedard-Hearn, R. E. Larsen, and B. J. Schwartz, J. Chem. Phys. **125**, 194509 (2006).
[51] D. T. Bowron, J. L. Finney, and A. K. Soper, J. Am. Chem. Soc. **128**, 5119 (2006).
[52] B. Winter, R. Weber, I. Hertel, M. Faubel, P. Jungwirth, E. C. Brown, and S. E. Bradforth, J. Am. Chem. Soc. **127**, 7203 (2005).
[53] G. Sciaini, R. Fernandez-Prini, D. A. Estrin, and E. Marceca, J. Chem. Phys. **126**, 174504 (2007).
[54] D. C. Sorensen, SIAM J. Matrix Anal. Appl. **13**, 357 (1992).
[55] K. Maschhoff and D. Sorensen, in *Applied Parallel Computing. Industrial Computation and Optimization. Third International Workshop, PARA '96 Proceedings*, 18–21 August 1996, Lyngby, Denmark, edited by J. Wasniewski, J. Dongarra, K. Madsen, and D. Olesen (Springer-Verlag, Berlin, 1996), pp. 478–86, ISBN 3 540 62095 8.
[56] P. Pulay, in *Applications of Electronic Structure Theory*, edited by H. F. S. Schaefer III (Plenum, New York, 1977).
[57] J. C. Phillips and L. Kleinman, Phys. Rev. **116**, 287 (1959).
[58] C. J. Smallwood, R. E. Larsen, W. J. Glover, and B. J. Schwartz, J. Chem. Phys. **125**, 074102 (2006).
[59] C. J. Smallwood, C. M. Mejia, W. J. Glover, R. E. Larsen, and B. J. Schwartz, J. Chem. Phys. **125**, 074103 (2006).
[60] F. Y. Jou and L. M. Dorfman, J. Chem. Phys. **58**, 4715 (1973).
[61] F. Webster, P. J. Rossky, and R. A. Friesner, Comput. Phys. Commun. **63**, 494 (1991).
[62] P. Mináry, L. Turi, and P. J. Rossky, J. Chem. Phys. **110**, 10953 (1999).
[63] L. Turi, G. Hantal, P. J. Rossky, and D. Boris, J. Chem. Phys. **131**, 024119 (2009).
[64] M. J. Bedard-Hearn, R. E. Larsen, and B. J. Schwartz, J. Phys. Chem. B **107**, 14464 (2003).
[65] J. Chandrasekhar and W. L. Jorgensen, J. Chem. Phys. **77**, 5080 (1982).
[66] J. M. Briggs, T. Matsui, and W. L. Jorgensen, J. Comput. Chem. **11**, 958 (1990).
[67] M. P. Allen and D. J. Tildesley, *Computer Simulation of Liquids* (Oxford University Press, London, 1992).
[68] O. Steinhauser, Mol. Phys. **45**, 335 (1982).
[69] W. A. Seddon, J. W. Fletcher, F. C. Sopchyshyn, and E. B. Selkirk, Can. J. Chem. **57**, 1792 (1979).

[70] Although the spectrum of sodide in Fig. 2 appears to show a dip at ~2.2 eV between the optically bright p-like states and the higher-lying states, we do not believe that this dip is a genuine feature as indicated by the overlapping error bars in the dip region and "peak" at 2.5 eV.
[71] The computational cost of evaluating Eq. (B6) limited us to calculating average projections for only the s,p and d SHs.
[72] The VBE is defined relative to the vacuum level. Although it would be useful to also know the location of the solvent conduction band relative

to the vacuum, determining the precise onset of the conduction band is complicated by the presence of solvent-supported disjoint electronic states below THF's conduction band (Refs. 27, 29, 31, 49, and 50). As we show in Sec. III B, our calculations reveal that these disjoint states mix with sodide's CTTS states, suggesting that the conduction band lies higher in energy than our calculated CTTS states.

[73] M. F. Fox and E. Hayon, J. Chem. Soc., Faraday Trans. 1 **73**, 1003 (1977).

[74] M. H. Cohen and V. Heine, Phys. Rev. **122**, 1821 (1961).

[75] D. R. Hamann, M. Schlüter, and C. Chiang, Phys. Rev. Lett. **43**, 1494 (1979).

[76] G. P. Kerker, J. Phys. C **13**, L189 (1980).

[77] N. Troullier and J. L. Martins, Phys. Rev. B **43**, 1993 (1991).

[78] The smoothing Gaussian width was chosen by considering the largest reciprocal-space vector supported by a Fourier-grid of $N=24$ in a simulation cell of 32.5 Å [the simulation parameters used in previous THF studies (Refs. 49 and 50)].

[79] Although the Mulliken charges on the THF sites differ from the partial charges used in the OPLS model (Ref. 66), the dipole moments resulting from both sets of charges agree to within 2%.

[80] H. Hotop and W. C. Lineberger, J. Phys. Chem. Ref. Data **14**, 731 (1985).